Geochemical Perspectives Letters EAG

Additive impact on early-stage magnesium carbonate mineralisation

F. Santoro De Vico[1], S. Bonilla-Correa[1], G. Pelayo-Punzano[1], K. Elert[1,2], C. Rodríguez-Navarro[1], E. Ruiz-Agudo[1*]

OPEN ACCESS
https://doi.org/10.7185/geochemlet.2441

Abstract

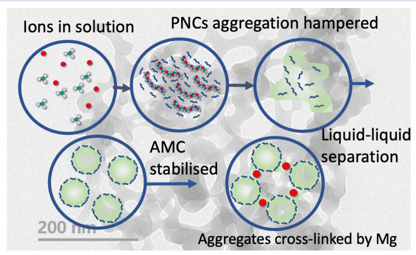

Carbon capture and utilisation has attracted significant interest due to increasing concerns about global warming. Mineral trapping *via* $MgCO_3$ precipitation is a promising strategy, though restricted by the slow rate of magnesite ($MgCO_3$) formation and high temperatures needed to avoid the formation of hydrated minerals. Amorphous magnesium carbonate (AMC) is a transient phase, determining the characteristics of the final crystalline $MgCO_3$ phase(s). Research has focused on accelerating $MgCO_3$ formation using additives, but their modus operandi is not completely understood. Here, AMC titration experiments were conducted at constant pH, monitoring solution transmittance, conductivity, and species size evolution to clarify the effect of citrate on the initial steps of $MgCO_3$ precipitation. We demonstrate that citrate, similar to more complex additives, alters the hydration of free ions relative to ion associates, thereby destabilising prenucleation ion associates and delaying AMC nucleation. The system is thus forced to go through liquid–liquid separation before the formation of the solid, resulting in amorphous and crystalline phases with lower water content, which are more stable and efficient for C storage, having a positive impact on the cost of CO_2 mineralisation.

Received 22 September 2023 | Accepted 8 September 2024 | Published 5 November 2024

Introduction

$MgCO_3$ minerals represent only a minor percentage of the carbonate deposits on the Earth. Consequently, fewer works have focused on magnesium carbonates compared to their calcium counterparts (Scheller *et al.*, 2021). Several anhydrous and hydrous minerals can be formed in the system, although magnesite ($MgCO_3$) is the thermodynamically stable phase (Hanchen *et al.*, 2008). However, for kinetic reasons it does not form under surficial *P–T* conditions. From an environmental point of view, carbonation processes are important since they reduce CO_2 concentration in the atmosphere and regulate the Earth's climate (*e.g.*, Berner *et al.*,1983). On the Earth's surface, carbonation occurs through chemical weathering of Ca^{2+}, Mg^{2+} and/or Fe^{2+} primary silicates. Although significant research has focused on mimicking this process for long-term CO_2 storage (MacDowell *et al.*, 2010; Bui *et al.*, 2018), this strategy is limited in the case of Mg-minerals due to the elevated temperature needed for the direct formation of magnesite and its slow rate of precipitation from solution.

Additionally, the synthesis of $MgCO_3$ with specific morphologies and structures such as rosette spheres (Zhang *et al.*, 2006), needle-like particles (Cheng, 2009) and mesoporous, nanostructured nanomaterials (*e.g.*, Baglioni and Giorgi, 2006), has been pursued for a broad variety of applications. Moreover, the mineral phase, morphology, and microstructural evolution of magnesium carbonates, formed upon carbonation of dolomitic lime, determine the physico-mechanical characteristics and functionality of mortars and plasters (*e.g.*, Elsen *et al.*, 2022; Oriols *et al.*, 2022).

In all the above applications, the early stages of $MgCO_3$ formation may significantly impact the stability, morphology and size of the final product. Research has focused on accelerating $MgCO_3$ formation by modifying the precipitation environment using additives (Toroz *et al.*, 2022 and references therein). Additives have been also suggested to lower the barrier for Mg^{2+} dehydration in solution (Toroz *et al.*, 2022), which could impact the water content of the final phase formed. Recent studies have shown that $MgCO_3$ precipitation is non-classic, and report the occurrence of amorphous magnesium carbonate (AMC) prior to the stable carbonate phase (White *et al.*, 2014; Tanaka *et al.*, 2019). The early stages of $MgCO_3$ formation via AMC remain, however, highly unexplored as compared to $CaCO_3$ (*e.g.*, Politi *et al.*, 2010; Rodriguez-Blanco *et al.*, 2011; Bots *et al.*, 2012; Rodriguez-Navarro *et al.*, 2015) and only a few studies have aimed at elucidating how these early stages are impacted by the presence of additives. Here, the synthesis of AMC was carried out at constant pH using a potentiometric titration setup. We aim at investigating the influence of sodium citrate, a low molecular weight additive, on the nucleation, growth, and stability of $MgCO_3$ phases.

1. Department of Mineralogy and Petrology, University of Granada, Fuentenueva s/n, Granada, 18002, Spain
2. Escuela de Estudios Árabes (EEA, CSIC), Cuesta del Chapiz 22, Granada, 18010, Spain
* Corresponding author (email: encaruiz@ugr.es)

Results and Discussion

Citrate inhibits AMC formation by destabilising prenucleation-associates. Titration experiments revealed the strong nucleation inhibition exerted by citrate. Solution transmittance (Fig. 1a) remained initially constant (425–450 mV) and, subsequently, a drop was observed that marked the onset of $MgCO_3$ formation (as AMC, see below). Citrate delayed the beginning of $MgCO_3$ precipitation. This effect can be best quantified using a scale factor that compares the increase in the time for nucleation relative to the control (additive-free) experiment, which showed a stronger inhibition—longer times for precipitation—with increasing citrate concentration (Fig. 1b). Interestingly, the transmittance plot showed different slopes after the precipitation onset, slopes being shallower at higher citrate concentrations.

Additionally, $MgCO_3$ precipitation can be tracked by conductivity measurements. Experimental data were compared to theoretical values (κ_{cal}, see Supplementary Information), showing significant deviation. Before precipitation, a continuous decrease in the conductivity of the solution was measured, while calculated values showed a steady increase due to the constant Mg^{2+} (and Cl^-) addition (Fig. 1c). This can be related to the development of ion associates in solution (*i.e.* any solution specie containing Mg^{2+} and CO_3^{2-}). While the formation of simple ion pairs in the system is certainly a possibility, previous results by Verch and co-workers showed the presence of ion associates larger than simple ion pairs during the early stages of $MgCO_3$ formation using analytical ultracentrifugation (AUC) (interpreted as prenucleation clusters, PNCs) (Verch *et al.*, 2012). The difference between κ and κ_{cal} could thus be used in the calculation of the concentration of $MgCO_3$ associates present in the solution (Fig. 1d) (see Supplementary Information). For citrate concentrations ≤0.1 mM, Mg-binding increased with citrate concentration. However, further increase in citrate concentration led to less pronounced Mg^{2+} binding into ion pairs and/or bigger associates, which are thus thermodynamically destabilised. It has been proposed that ion association prior to nucleation is predominantly driven by entropy, and not by energy release associated with ionic binding (Kellermeier *et al.*, 2016); the release of coordination water upon ion association represents the main entropic contribution, related to the increase in H_2O translational and rotational degrees of freedom (Kellermeier *et al.*, 2016). This entropic contribution is expected to be key in the case of Mg^{2+} due to its strongly hydrated character. However, atomistic simulations (Toroz *et al.*, 2022) have shown that citrate promotes Mg^{2+} dehydration; thus, in this

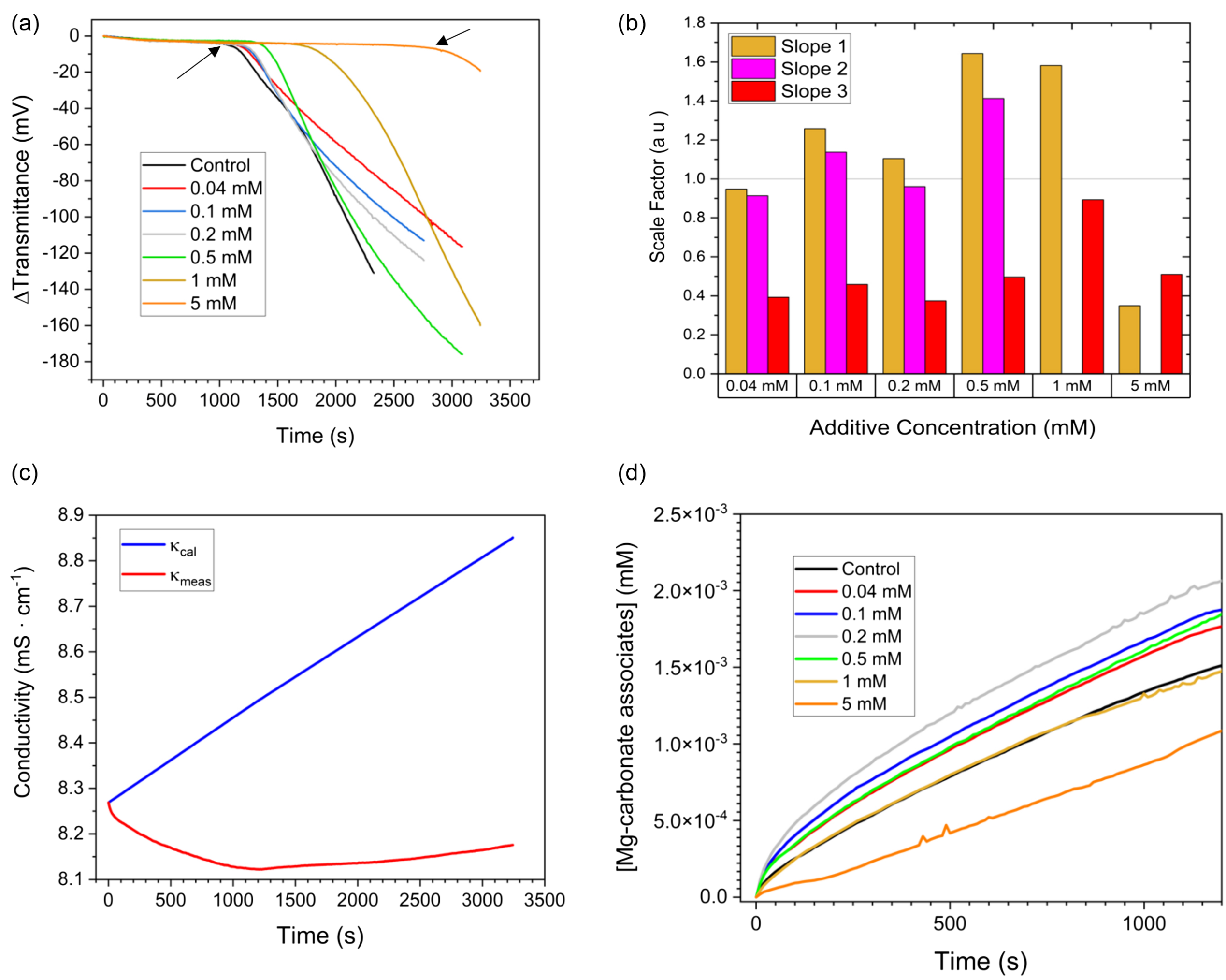

Figure 1 Results of titration experiments. **(a)** Evolution of transmittance in the presence of citrate at pH 11. Black arrows mark the point at which samples were taken for transmission electron microscopy (TEM) analysis. **(b)** Bar plot illustrating the effect of citrate on the different slopes of the decreasing part of the transmittance curve. **(c)** Time evolution of calculated (blue line) and measured (red line) conductivity. **(d)** Evolution of the calculated concentration of ion associates in the presence of different amounts of citrate at pH 11. For details on the calculation see Supplementary Information.

case, the entropy gain associated with Mg-CO_3 associates formation—relative to the free ions in solution—would be lower than when no additive is present, making the development of Mg-CO_3 associates in solution less favourable. The pronounced nucleation inhibition of citrate highlights: (i) the importance of dehydration events for solute clustering, and (ii) the key role of $MgCO_3$ binding in prenucleation associates for AMC nucleation.

After the precipitation onset, the measured conductivity started increasing, but it was still lower than the calculated conductivity, due to ion incorporation in the solid during growth. Assuming a 1:1 Mg^{2+} to CO_3^{2-} ratio in the solid, and a constant concentration of ion associates in equilibrium with the solid, the growth rate can be determined as the ratio of the difference between theoretical and experimental conductivity and the molar specific conductivity. Values are plotted in Figure S-1, where it is observed that citrate inhibited AMC growth at higher concentrations, while showing a slight trend to promote growth at low concentration.

In situ dynamic light scattering (DLS) measurements provided data on the size evolution of pre- and post-nucleation species formed during titration experiments (Fig. 2). In control runs, species with a hydrodynamic radius between 5–10 nm were observed during the prenucleation regime. We interpret these species as aggregates of ion associates, possibly pre-nucleation clusters. The size range was slightly higher than that reported for $CaCO_3$ (Gebauer *et al.*, 2014), in agreement with the larger sedimentation coefficients reported for $MgCO_3$ PNCs (Verch *et al.*, 2012; Gebauer *et al.*, 2014). Subsequently, the size of the solution species remained between 2 and 20 nm. It is unlikely that such fast particle growth was exclusively due to the growth of single particles, but most probably caused by continued nanoparticle aggregation. No significant change in size was observed upon nucleation of solid $MgCO_3$ in control runs (see dotted red line in Fig. 2c).

In the case of citrate, smaller clusters (approximately 2 nm) were initially observed, which rapidly grow up to 40 nm, with a broader size distribution. These features align with the formation of a liquid precursor upon spinodal decomposition (see below). Prior to the onset of solid $MgCO_3$ nucleation, a continuous decrease in the size of the entities in solution down to 5–10 nm was observed. This could be due to the dehydration of the dense liquid-like phase (see below) and AMC nucleation. At longer reaction times ($t > 3500$ s), aggregates of sizes from 1 to 5 µm were observed, not detected in the control runs. Similar trends were observed for a 5 mM citrate concentration, but

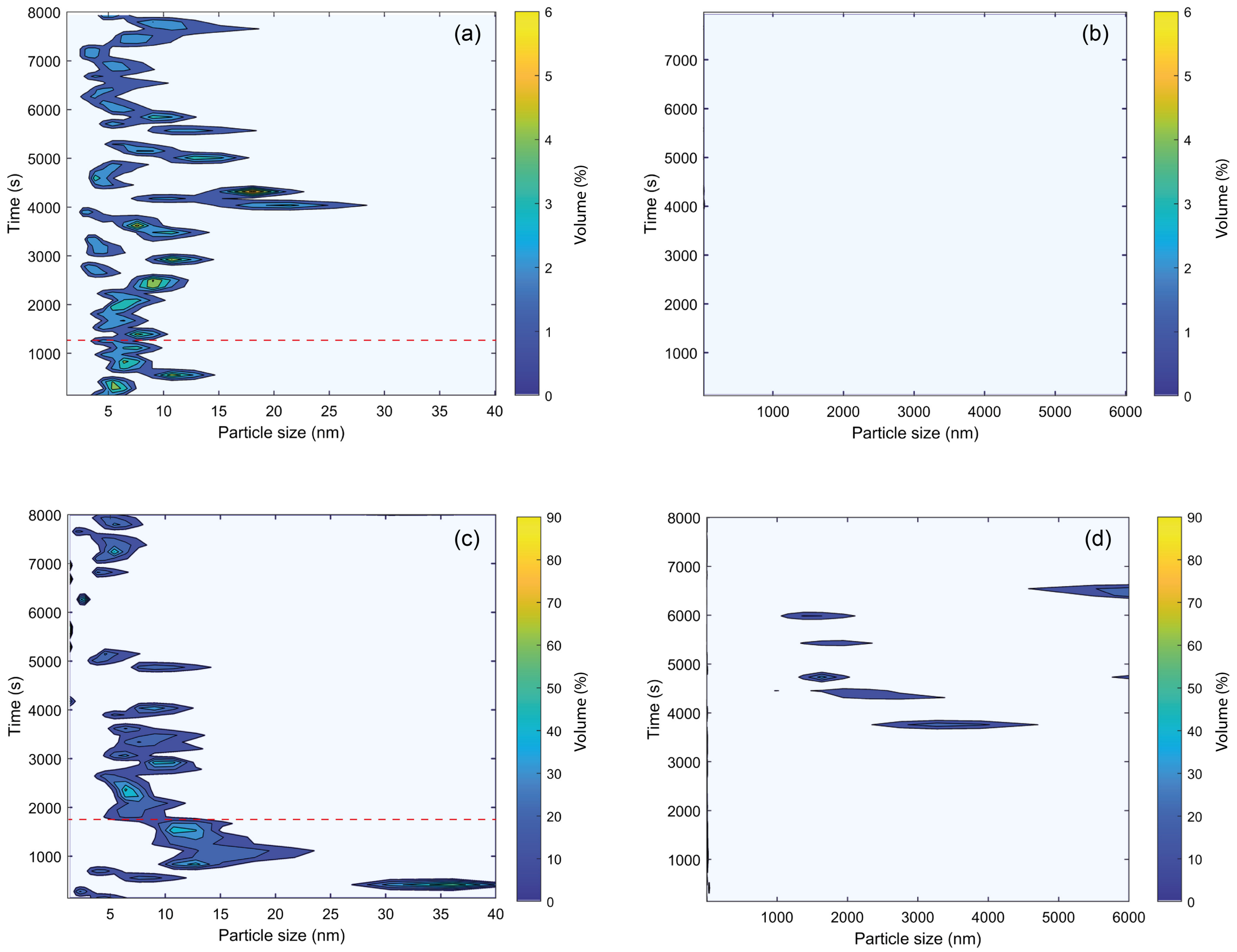

Figure 2 Size evolution of the different (pre- and post-nucleation) species formed during titration experiments obtained by *in situ* dynamic light scattering (DLS): **(a)** size range from 0 to 40 nm, control runs; **(b)** size range from 0 to 6000 nm, control runs; **(c)** size range from 0 to 40 nm, experiments in the presence of 1 mM citrate; **(d)** size range from 0 to 6000 nm, experiments in the presence of 1 mM citrate. Onset of nucleation is marked with a red line.

the size of the different species observed was significantly larger (Fig. S-2). This size agrees with that of the individual aggregates observed by FESEM (Fig. 3). We propose that, as it has been shown in the case of Au nanoparticle stabilisation by citrate (Park and Shumaker-Parry, 2014), its binding to the surface of AMC nanoparticles leads to the formation of 1-D citrate chains, which assemble into layers through van der Waals interactions, leading to steric repulsion between citrate layers that prevent the initial aggregation of AMC nanoparticles. We have detected such layers in the case of citrate-stabilised amorphous calcium oxalate (Ruiz-Agudo *et al.*, 2017). However, with increasing Mg^{2+} concentration, complexation between Mg^{2+} ions and these citrate chains may contribute to crosslinking AMC nanoparticles and promote the formation of μm-sized aggregates (Fig. 4). These observations can explain the different slopes observed in the transmittance plot (Fig. 1a) after the onset of precipitation, likely corresponding to different regimes of the growth and/or aggregation of AMC nanoparticles. The shallower slopes observed in the presence of citrate agree with the observed growth inhibition and the retardation of nanoparticle aggregation/growth determined from conductivity and particle size measurements.

Finally, aliquots collected shortly after the first drop in transmittance slope were quenched in ethanol and analysed using transmission electron microscopy (TEM) and selected area electron diffraction (SAED) (Fig. 3). Shapeless structures with irregular morphologies were observed when citrate was added to the solution, resembling aggregates of spherical nanoparticles with darker contrast, connected by neck-like bridges with lighter contrast, similar to those observed during $CaCO_3$ (*e.g.*, Rodriguez-Navarro *et al.*, 2015) or $CaPO_4$ precipitation (Ruiz-Agudo *et al.*, 2021). SAED confirmed their amorphous nature, interpreted as being a dried residue of an emulsion (liquid-like) precursor phase formed after spinodal decomposition, as stated above, which subsequently transforms into AMC particles (for further details on this process, see Rodriguez-Navarro *et al.*, 2015 or Ruiz-Agudo *et al.*, 2021 and references therein). Remarkably, these distinct structures were not observed in the control samples. The diffuse rings observed in the SAED pattern of both control and citrate bearing AMCs at ~1.5Å, ~2.0 Å and at ~2.5 Å match the (160), (240) and (230) *d*-spacings of hydromagnesite, which suggests that AMC could have a hydromagnesite-like protostructure, in agreement with previous reports (Yamamoto *et al.*, 2021).

***Ex-situ* characterisation of $MgCO_3$ precipitates.** Powder X-ray diffraction (XRD) confirmed that the precipitates formed at the end of the titration runs (Fig. S-3), with and without citrate, are amorphous. After ageing for one week in the reaction media, AMC recrystallised into nesquehonite ($MgCO_3{\cdot}3H_2O$) and dypingite ($Mg_5(CO_3)_4(OH)_2{\cdot}5H_2O$), in the absence and in the presence of citrate, respectively (Fig. S-3). Figure S-4 shows the Fourier transform infrared (FTIR) spectra of precipitates. In control precipitates, broad absorption bands corresponding to CO_3^{2-} were observed at 835 cm^{-1}, 1024 cm^{-1} and 1389 cm^{-1} (White, 1971; Zhang *et al.*, 2006). In addition, the O-H bending and stretching modes of water gave rise to a low intensity shoulder at 1644 cm^{-1} and a broad band observed in the 3000 cm^{-1} range. The weak, broad shoulder observed at 3664 cm^{-1} (not seen in the presence of citrate) could be linked to OH^- groups present in the control AMC. The broad features observed, in addition to the presence of the band at 1024 cm^{-1} and the absence of the band at ~748 cm^{-1}, support the amorphous nature of the precipitates, when compared to the sharper,

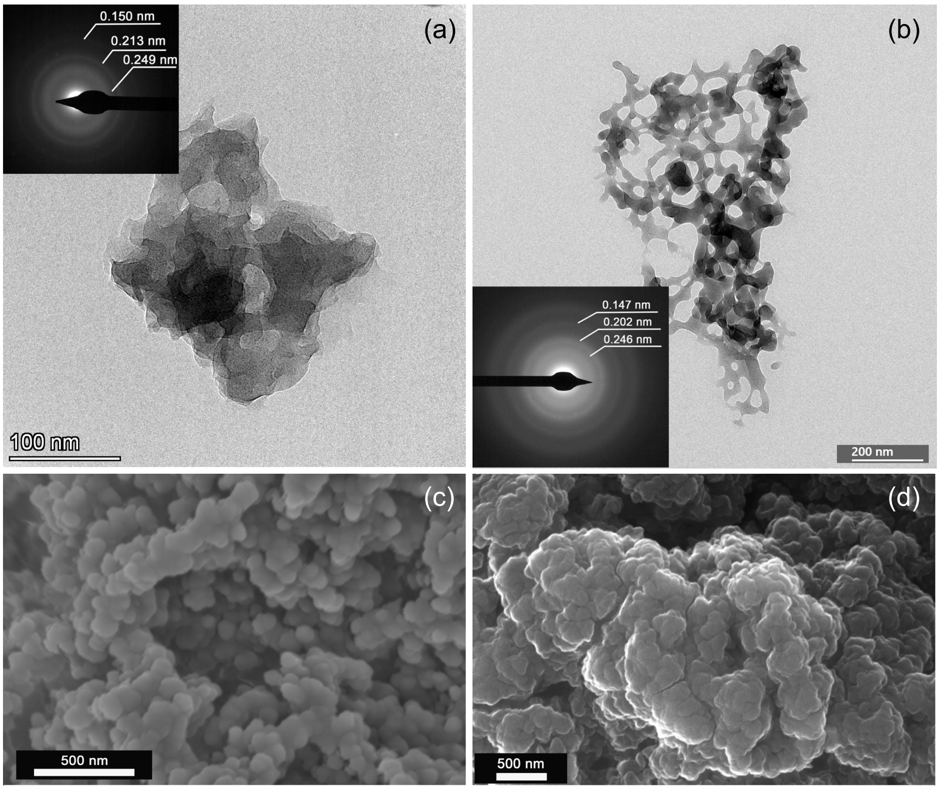

Figure 3 Nanostructural features of the pre- and post-nucleation species. **(a, b)** TEM images and SAED patterns of dried aliquots drawn from the solution immediately prior to the onset of nucleation—**(a)** control runs and **(b)** sodium citrate 1 mM experiments. **(c, d)** FESEM secondary electron images of the final precipitates—**(c)** control runs and **(d)** sodium citrate 1 mM experiments—separated by filtration from the reaction media at the end of the titration experiments.

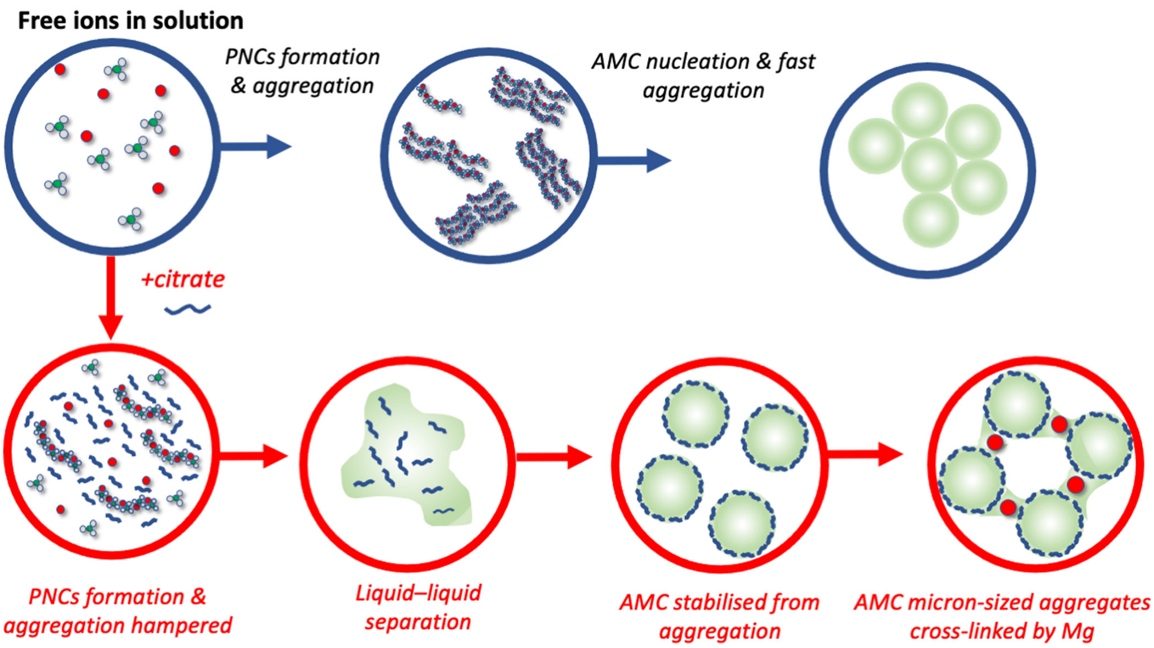

Figure 4 Scheme of the multi-step formation of AMC in control solutions (blue circles, no additives in the media) and in the presence of sodium citrate (red circles).

better defined features of the FTIR spectra of crystalline $MgCO_3$ (White, 1971; Zhang *et al.*, 2006; Tanaka *et al.*, 2019). Citrate absorption bands (Mudunkotuwa and Grassian, 2010) overlapped with carbonate bands, and were not observed. However, carbonate bands were blue-shifted to 858, 1084 and 1402 cm^{-1} in the presence of citrate; this could be explained by citrate-Mg interactions that weaken Mg-CO_3 bonding in the $MgCO_3$ phase, thus increasing the strength of C-O bonds. Also, the subtle red-shift found in the O-H vibration bands could indicate citrate-OH bonding.

Thermogravimetric analysis (TGA) of control AMC showed two main weight losses (Fig. S-5a), associated with AMC dehydration (~280 °C) and decarbonation (280–950 °C) (Radha *et al.*, 2012). In the case of citrate-bearing AMC, two dehydration steps were seen, suggesting that water exists in different environments. The second step was observed at higher temperatures, indicating that part of the water is more tightly bonded in the presence of citrate. TGA revealed that control AMC contained 1.82 ± 0.17 moles of water per mole of $MgCO_3$, which is in the range of values previously reported (1.28–2) (*e.g.*, Radha *et al.*, 2012; Tanaka *et al.*, 2019; (Yamamoto et al., 2021)). This phase plots close to dypingite in the ternary diagram of hydrated $MgCO_3$ (Fig. S-6). The water content of AMC was reduced for the lowest citrate concentrations (Fig. S-6). This could be related to the fact that carboxylate anions lower the barrier for Mg^{2+} dehydration in solution by stabilising undercoordinated Mg^{2+} hydration configurations, as shown by recent molecular simulations (Toroz *et al.*, 2022). The differential scanning calorimetry (DSC) profile of AMC (Fig. S-5b) showed two endothermic events at 130 °C and 430 °C, corresponding to dehydration and decarbonation, respectively. Since no other thermal event was detected, it is clear that AMC decomposes without crystallisating. TGA and DSC results showed an increase in decarbonation temperature (*ca.* 100 °C) in the presence of citrate, which suggests that the dehydrated AMC is more stable. Finally, zeta potential values were negative in all AMC samples (Table S-1). The presence of OH^- groups in the structure can explain such values. The less negative values of the citrate-bearing AMC could be related with its lower degree of hydration, possibly associated with its lower OH^- content.

Conclusions and Implications

We propose that $MgCO_3$ solution species form by Mg^{2+} and CO_3^{2-} association, driven by the entropy gain linked to the release of coordination water, and subsequent grow by aggregation prior to the beginning of AMC nucleation (Fig. 4). $-COO^-$ in citrate can lower the barrier for Mg^{2+} dehydration by stabilising undercoordinated Mg^{2+} hydration configurations, as shown by molecular simulations (Toroz *et al.*, 2022 and references therein). The entropy gain associated with water removal during Mg^{2+} and CO_3^{2-} association will thus be lower than in the absence of citrate, making Mg^{2+} binding in the pre-nucleation ion associates less favourable. Formation of ion associates and subsequent aggregation are key processes for AMC nucleation, and both are hampered by citrate. This inhibits AMC nucleation, so that the system passes the spinodal limit leading to the formation of a dense liquid-like precursor. This is technologically relevant, since a small-weight, environmentally friendly carboxylic acid, such as citrate, bears similar effects as more complex polymers, and can potentially be used to precipitate particles with intricate morphologies. Moreover, low concentrations of citrate (<1 mM) accelerate AMC growth and reduce the water content of AMC, resulting in the formation of less hydrated crystalline $MgCO_3$ phases, as is the case of dypingite, as opposed to nesquehonite formed after AMC in the absence of citrate. Citrate works similarly in other mineral systems, which could be linked to its high radial charge density that enables its interaction with ions in solution, promoting Mg^{2+} (or other cations or ion associates) dehydration. This could have a significant impact on mineralisation where cation dehydration is an essential step. Less hydrated Mg-carbonate phases are more stable and efficient as carbon storage medium compared to highly hydrated phases, due to the lower mass and volume per mole of CO_2 stored and the greater chemical stability/lower solubility, suitable for long-term storage, ultimately having a positive effect on the effectiveness and expense of CO_2 mineralisation (Swanson *et al.*, 2014).

Acknowledgements

This research has been funded by the EC (ACT_ERA NET no. 691712, PCI2019-111931-2 and H2020 Programme, Marie Skłodowska-Curie Action ETN-ITN SUBlime, grant agreement n° 955986), the Spanish Government (grant PID2021-125305NB-I00), Junta de Andalucía (research group RNM-179 and grant P20_00675) and University of Granada (Unidad Científica de Excelencia UCE-PP2016-05).

Editor: Satish Myneni

Additional Information

Supplementary Information accompanies this letter at https://www.geochemicalperspectivesletters.org/article2441.

Cite this letter as: Santoro De Vico, F., Bonilla-Correa, S., Pelayo-Punzano, G., Elert, K., Rodríguez-Navarro, C., Ruiz-Agudo, E. (2024) Additive impact on early-stage magnesium carbonate mineralisation. *Geochem. Persp. Let.* 32, 46–51. https://doi.org/10.7185/geochemlet.2441

References

Baglioni, P., Giorgi, R. (2006) Soft and hard nanomaterials for restoration and conservation of cultural heritage. *Soft Matter* 2, 293–303. https://doi.org/10.1039/b516442g

Berner, R.A., Lasaga, A.C., Garrels, R.M. (1983) The Carbonate-Silicate Geochemical Cycle and Its Effect on Atmospheric Carbon-Dioxide over the Past 100 Million Years. *American Journal of Science* 283, 641–683. https://doi.org/10.2475/ajs.283.7.641

Bots, P., Benning, L.G., Rodriguez-Blanco, J.D., Roncal-Herrero, T., Shaw, S. (2012) Mechanistic Insights into the Crystallization of Amorphous Calcium Carbonate (ACC). *Crystal Growth & Design* 12, 3806–3814. https://doi.org/10.1021/cg300676b

Bui, M., Adjiman, C.S., Bardow, A., Anthony, E.J., Boston, A., Brown, S., Fennell, P.S., Fuss, S., Galindo, A., Hackett, L.A., Hallett, J.P., Herzog, H.J., Jackson, G., Kemper, J., Krevor, S., Maitland, G.C., Matuszewski, M., Metcalfe, I.S., Petit, C., Puxty, G., Reimer, J., Reiner, D.M., Rubin, E.S., Scott, S.A., Shah, N., Smit, B., Trusler, J.P.M., Webley, P., Wilcox, J., Mac Dowell, N. (2018) Carbon capture and storage (CCS): the way forward. *Energy & Environmental Science* 11, 1062–1176. https://doi.org/10.1039/C7EE02342A

Cheng, W.T., Li, Z.B., Demopoulos, G.P. (2009) Effects of Temperature on the Preparation of Magnesium Carbonate Hydrates by Reaction Of MgCl2 with Na2CO3. *Chinese Journal of Chemical Engineering* 17, 661–666. https://doi.org/10.1016/S1004-9541(08)60260-8

Elsen, J., Jackson, M.D., Ruiz-Agudo, E. (2022) Historic Concrete Science: Opus Caementicium to "Natural Cements". *Elements* 18, 301–307. https://doi.org/10.2138/gselements.18.5.301

Gebauer, D., Kellermeier, M., Gale, J.D., Bergstrom, L., Colfen, H. (2014) Pre-nucleation clusters as solute precursors in crystallisation. *Chemical Society Reviews* 43, 2348–2371. https://doi.org/10.1039/C3CS60451A

Hanchen, M., Prigiobbe, V., Baciocchi, R., Mazzotti, M. (2008) Precipitation in the Mg-carbonate system - effects of temperature and CO2 pressure. *Chemical Engineering Science* 63, 1012–1028. https://doi.org/10.1016/j.ces.2007.09.052

Kellermeier, M., Raiteri, P., Berg, J.K., Kempter, A., Gale, J.D., Gebauer, D. (2016) Entropy Drives Calcium Carbonate Ion Association. *ChemPhysChem* 17, 3535–3541. https://doi.org/10.1002/cphc.201600653

MacDowell, N., Florin, N., Buchard, A., Hallett, J., Galindo, A., Jackson, G., Adjiman, C.S., Williams, C.K., Shah, N., Fennell, P. (2010) An overview of CO2 capture technologies. *Energy & Environmental Science* 3, 1645–1669. https://doi.org/10.1039/c004106h

Mudunkotuwa, I.A., Grassian, V.H. (2010) Citric Acid Adsorption on TiO_2 Nanoparticles in Aqueous Suspensions at Acidic and Circumneutral pH: Surface Coverage, Surface Speciation, and Its Impact on Nanoparticle-Nanoparticle Interactions. *Journal of the American Chemical Society* 132, 14986–14994. https://doi.org/10.1021/ja106091q

Oriols, N., Salvado, N., Pradell, T., Jimenez, N., Cotte, M., Gonzalez, V., Buti, S. (2022) Carbonation of fresco mural paintings with a dolomitic mortar. *Cement and Concrete Research* 157. https://doi.org/10.1016/j.cemconres.2022.106828

Park, J.-W., Shumaker-Parry, J.S. (2014) Structural study of citrate layers on gold nanoparticles: role of intermolecular interactions in stabilizing nanoparticles. *Journal of the American Chemical Society*. 36, 1907–1921. https://pubs.acs.org/doi/10.1021/ja4097384

Politi, Y., Batchelor, D.R., Zaslansky, P., Chmelka, B.F., Weaver, J.C., Sagi, I., Weiner, S., Addadi, L. (2010) Role of Magnesium Ion in the Stabilization of Biogenic Amorphous Calcium Carbonate: A Structure-Function Investigation. *Chemistry of Materials* 22, 161–166. https://doi.org/10.1021/cm902674h

Radha, A.V., Fernandez-Martinez, A., Hu, Y.D., Jun, Y.S., Waychunas, G.A., Navrotsky, A. (2012) Energetic and structural studies of amorphous $Ca_{1-x}Mg_xCO_3{\cdot}nH_2O$ ($0 \leq x \leq 1$). *Geochimica Et Cosmochimica Acta* 90, 83–95. https://doi.org/10.1016/j.gca.2012.04.056

Rodriguez-Blanco, J.D., Shaw, S., Benning, L.G. (2011) The kinetics and mechanisms of amorphous calcium carbonate (ACC) crystallization to calcite, via vaterite. *Nanoscale* 3, 265–271. https://doi.org/10.1039/C0NR00589D

Rodriguez-Navarro, C., Kudlacz, K., Cizer, O., Ruiz-Agudo, E. (2015) Formation of amorphous calcium carbonate and its transformation into mesostructured calcite. *CrystEngComm* 17, 58–72. https://doi.org/10.1039/C4CE01562B

Ruiz-Agudo, E., Burgos-Cara, A., Ruiz-Agudo, C., Ibanez-Velasco, A., Colfen, H., Rodriguez-Navarro, C. (2017) A non-classical view on calcium oxalate precipitation and the role of citrate. *Nature Communications* 8, 768. https://doi.org/10.1038/s41467-017-00756-5

Ruiz-Agudo, E., Ruiz-Agudo, C., Di Lorenzo, F., Alvarez-Lloret, P., Ibanez-Velasco, A., Rodriguez-Navarro, C. (2021) Citrate Stabilizes Hydroxylapatite Precursors: Implications for Bone Mineralization. *ACS Biomaterials Science & Engineering* 7, 2346–2357. https://doi.org/10.1021/acsbiomaterials.1c00196

Scheller, E.L., Swindle, C., Grotzinger, J., Barnhart, H., Bhattacharjee, S., Ehlmann, B.L., Farley, K., Fischer, W.W., Greenberger, R., Ingalls, M., Martin, P.E., Osorio-Rodriguez, D., Smith, B. (2021) Formation of Magnesium Carbonates on Earth and Implications for Mars. *Journal of Geophysical Research-Planets* 126. https://doi.org/10.1029/2021JE006828

Swanson, E.J., Fricker, K.J., Sun, M., Park, A.H. (2014) Directed precipitation of hydrated and anhydrous magnesium carbonates for carbon storage. *Physical Chemistry Chemical Physics* 16, 23440–234450. https://doi.org/10.1039/C4CP03491K

Tanaka, J., Kawano, J., Nagai, T., Teng, H. (2019) Transformation process of amorphous magnesium carbonate in aqueous solution. *Journal of Mineralogical and Petrological Sciences* 114, 105–109. https://doi.org/10.2465/jmps.181119b

Toroz, D., Song, F., Uddin, A., Chass, G.A., Di Tommaso, D. (2022) A Database of Solution Additives Promoting Mg^{2+} Dehydration and the Onset of $MgCO_3$ Nucleation. *Crystal Growth & Design* 22, 3080–3089. https://doi.org/10.1021/acs.cgd.1c01525

Verch, A., Antonietti, M., Colfen, H. (2012) Mixed calcium-magnesium pre-nucleation clusters enrich calcium. *Zeitschrift Fur Kristallographie-Crystalline Materials* 227, 718–722. https://doi.org/10.1524/zkri.2012.1529

White, C.E., Henson, N.J., Daemen, L.L., Hartl, M., Page, K. (2014) Uncovering the True Atomic Structure of Disordered Materials: The Structure of a Hydrated Amorphous Magnesium Carbonate ($MgCO_3{\cdot}3D_2O$). *Chemistry of Materials* 26, 2693–2702. https://doi.org/10.1021/cm500470g

White, W.B. (1971) Infrared Characterization of Water and Hydroxyl Ion in Basic Magnesium Carbonate Minerals. *American Mineralogist* 56, 46–53.

Yamamoto, G., Kyono, A., Okada, S. (2021) Temperature dependence of amorphous magnesium carbonate structure studied by PDF and XAFS analyses. *Scientific Reports* 11. https://doi.org/10.1038/s41598-021-02261-8

Zhang, Z.P., Zheng, Y.J., Ni, Y.W., Liu, Z.M., Chen, J.P., Liang, X.M. (2006) Temperature- and pH-dependent morphology and FT-IR analysis of magnesium carbonate hydrates. *Journal of Physical Chemistry B* 110, 12969–12973. https://doi.org/10.1021/jp061261j

Geochemical Perspectives Letters EAG

Additive impact on early-stage magnesium carbonate mineralisation

F. Santoro De Vico, S. Bonilla-Correa, G. Pelayo-Punzano, K. Elert, C. Rodríguez-Navarro, E. Ruiz-Agudo

Supplementary Information

The Supplementary Information includes:

- Methodology
- Figures S-1 to S-6
- Table S-1
- Supplementary Information References

Methodology

In situ monitoring of $MgCO_3$ precipitation.

$MgCO_3$ precipitation experiments were carried out at a fixed pH of 11, maintained by NaOH addition using a Titrino 905 (Methrom). A 100 mM magnesium chloride (Sigma Aldrich, anhydrous, ≥98 %) solution was continuously added at a rate of 0.12 mL min^{-1} to a 50 mM potassium carbonate (Sigma Aldrich, anhydrous, free-flowing, Redi-Dri™, ACS reagent, ≥99 %) buffer. Tri-sodium citrate dihydrate (Sigma Aldrich, ACS, ISO, Reag. Ph Eur; 0.04 to 5 mM) was added to the carbonate buffer. Each titration experiment was performed at least in triplicate (10 times for runs without additives) for representativity. pH, solution conductivity and transmittance were monitored during the duration of the experiments using a glass electrode, a conductometric cell and a photometric sensor equipped with a laser at a wavelength of 610 nm by Metrohm, respectively. The cell constant of the conductivity probe was determined by measurement of an electrolyte solution with known conductivity (in this case, 0.01 and 0.1 M potassium chloride standard solutions, with a conductivity of 1.41 mS/cm and 12.88 mS/cm, respectively). *In situ*, continuous monitoring of the evolution of particle size evolution was performed by dynamic light scattering (DLS), using a Microtrac NANO-flex analyzer. The system consists of a 780 nm diode laser with 5 mW power and a probe with sapphire window and a length of 1 m and diameter of 8 mm. Each run was acquired during 45 s, with an elapsed time between measurements of 20 s. The Microtrac FLEX software (v.11.1.0.1) was used for determination of particle size distributions. Finally, we performed zeta potential analysis of AMC samples using a Microtrac Zeta-check particle charge analyser. 3 mL of the reaction media were taken directly from the reactor of the titration system in two different points of the transmittance curve (immediately after the first drop of the transmittance plot and upon the transmittance of the solution has stabilised) and immediately analyzed for zeta potential. Additionally, at the end of the titration experiments, 50 mg of the filtered and dried precipitates were re-suspended in MilliQ® water, sonicated during 2 minutes for homogenization and dispersion of the AMC, and zeta potential measurements were immediately performed (six measurements within the first two minutes, and two more three and five minutes after sonication, respectively), to ensure the robustness and representativeness of the results.

Theoretical electrical conductivity values (κ_{cal}) for the reaction solutions can be calculated following the protocol described in previous works (Ruiz-Agudo *et al*. 2017, 2021). In this work, the ionic molal conductivity (λ) of all ions was calculated using equation:

$$\lambda_i = \lambda_i^{\circ}(T) - \frac{A(T)I^{\frac{1}{2}}}{1+BI^{\frac{1}{2}}} \qquad \textit{Eq .S-1}$$

where $\boldsymbol{\lambda_i^{\circ}}$ and A are functions of temperature (T, ºC), B is an empirical constant and I is the ionic strength of the solution. Equations for $\boldsymbol{\lambda_i^{\circ}}$ and A calculation and B values for different ions can be found in (McCleskey et al., 2012). I, which is a measure of the concentration of all charged ions in solution, can be calculated using:

$$I = \frac{1}{2}\sum m_i z_i^2 \qquad \textit{Eq. S-2}$$

where z_i is the charge of the i^{th} ion. Since $\boldsymbol{\lambda_i^{\circ}}$ and A functions and B value for citrate are not available in the literature, and considering the dilute character of the solutions, we used the (constant) value of ionic molar conductivity reported in Lide (2004) as the ionic molal conductivity of citrate (210.6 mS kg cm^{-1} mol^{-1}).

This calculation gives higher κ_{cal} than the actual measured values (κ) (Fig. 1c), as a result of the ion clustering before nucleation:

$$\kappa = \kappa_{\mathrm{cal}} - c_{MgCO_3}\lambda_{\mathrm{MgCO_3}} \qquad \textit{Eq.}\ \text{S-4}$$

where $\boldsymbol{c_{\mathrm{MgCO_3}}}$ is the concentration of pre-nucleation $MgCO_3$ associates and $\boldsymbol{\lambda_{\mathrm{MgCO_3}}}$ is the molal conductivity of $MgCO_3$ associates, estimated using the Kohlrausch law which considers that the molal conductivity of an electrolyte is given by the ionic molal conductivity of its components using the following equation:

$$\boldsymbol{\lambda_{MgCO_3} = \lambda_{Mg^{2+}} + n \cdot \lambda_{CO_3^{2-}}} \qquad \textit{Eq. S-5}$$

where n is a dimensionless number corresponding to the ratio of anions to cations in the $MgCO_3$ prenucleation associates. The exact value of n can be determined by comparison with the concentration of pre-nucleation $MgCO_3$ associates determined from Mg activity measurements (*e.g*., Ruiz-Agudo *et al*., 2017, 2021). However, such measurements were not reliable in our system under the experimental conditions selected since they were not able to show any decrease in free Mg^{2+} activity upon solid formation, detected from changes in conductivity and transmittance measurements. Considering n=1 as in the $CaCO_3$-H_2O system, $\boldsymbol{c_{\mathrm{MgCO_3}}}$ was calculated (Fig. 1d) for control runs and solutions containing citrate. Calculations performed with n values of 2 and 3 led to similar trends, *i.e*. enhanced Mg^{2+} binding at the lower citrate concentration, less pronounced Mg^{2+} binding in PNCs for citrate > 0.1 mM (data not shown). Note that this calculation yields maximum concentration values, since Mg-binding by citrate is not considered.

Finally, 1 mL of the reaction media was drawn immediately before nucleation (indicated by the first steep fall in the solution transmittance, after ca. 1000 s and 2800 s for the control and 1 mM citrate solution, respectively -see black arrows in Fig. 1a in the main text-) and poured into a mixture of 75 % acetone and 25 % absolute ethanol contained in a plastic beaker that was afterwards sealed with Parafilm™. Drops of the resulting dispersion were deposited on carbon coated Cu grids prior to TEM observation using a FEI Titan, (300 kV) and a 30 µm objective aperture. A 10 µm aperture was used to obtained selected area electron diffraction (SAED) patterns from a circular area of a diameter ~0.2 µm. A Super X EDS detector (FEI) consisting of four SSD detectors with no window surrounding the sample was used to record compositional maps in STEM mode of representative areas of the samples, while STEM images were collected using a high-angle annular dark field (HAADF) detector.

Ex-situ analysis of precipitates.

Once the precipitation experiment was completed, the reaction media was filtered using Nucleopore membranes (ϕ = 200 nm) to separate the solids, which were subsequently analyzed by X-ray diffraction using a PANalytical X'Pert Pro X-ray diffractometer. Diffraction patterns were collected using Cu Kα radiation (λ = 1.5405 Å), from 3 to 50° 2θ range, at a scanning rate of 0.11° 2θ s^{-1}. Further characterisation was performed by Fourier Transform Infrared spectroscopy (FTIR) using an ATRproONE-FTIR spectrometer from Jasco (Model 6600) in the frequency range 400-4000 cm^{-1}, with a resolution of 2 cm^{-1} and 100 accumulations, and thermogravimetry and differential scanning calorimetry (TGA/DSC;) with a Mettler-Toledo TGA/DSC equipment in the temperature range 25-950 °C, at a heating rate of 10 K/min, with flowing air at 120 mL/min.

Supplementary Figures

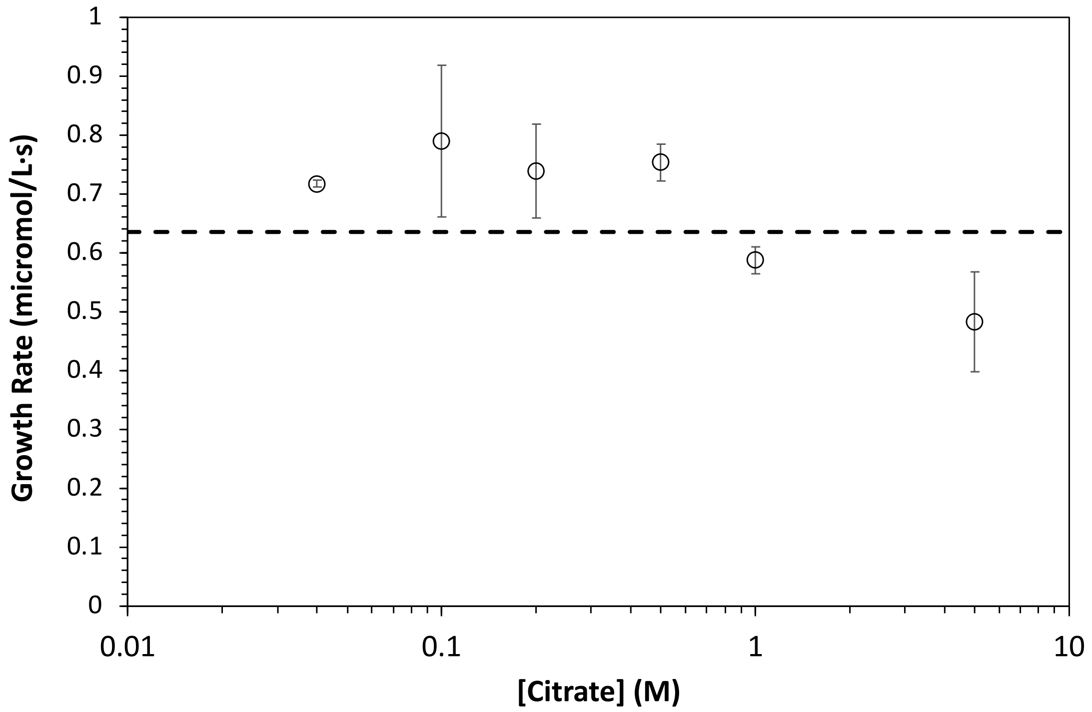

Figure S-1 AMC growth rate *vs.* citrate concentration determined from conductivity measurements as the ratio of the difference between theoretical and experimental conductivity and the molar specific conductivity of $MgCO_3$, assuming a 1:1 Mg^{2+} to CO_3^{2-} ratio in the solid. The dotted horizontal line represents the growth rate determined in the absence of citrate.

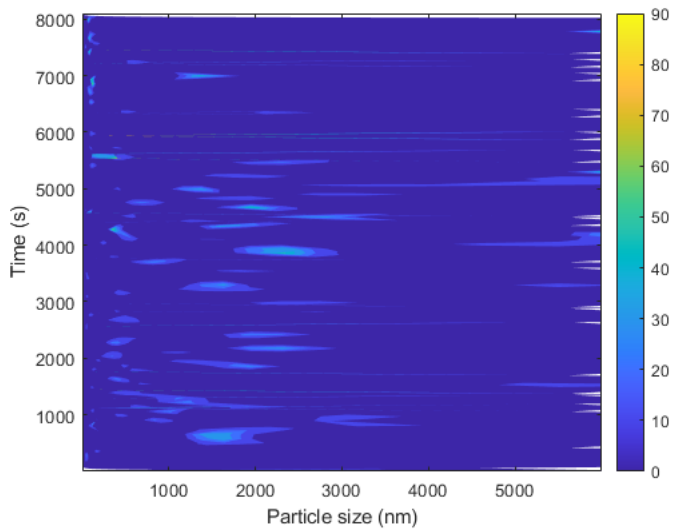

Figure S-2 Size evolution of the different (pre- and post-nucleation) species formed during titration experiments obtained by *in situ* dynamic light scattering (DLS) in the presence of 5 mM citrate.

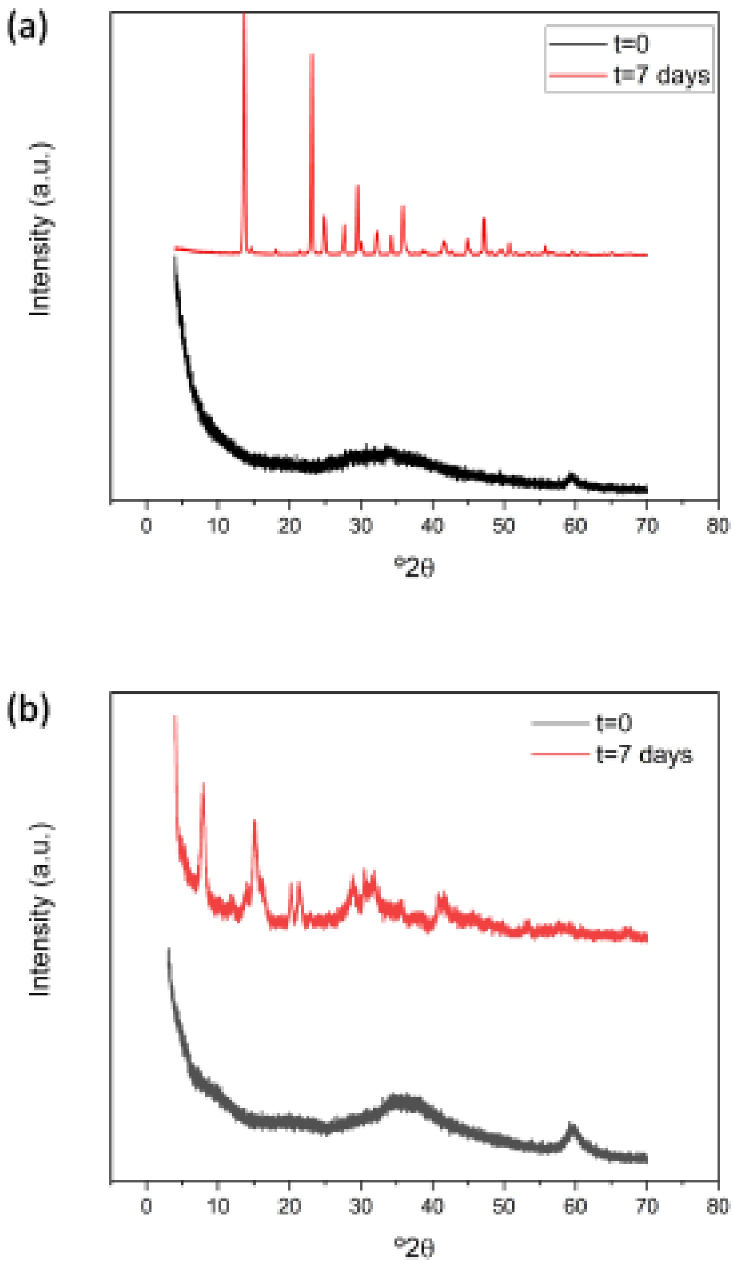

Figure S-3 XRD pattern of precipitates formed immediately after titration experiments (black plot) and after one week in the reaction media under constant stirring at 25 ºC (red plot). The absence of any diffraction peaks in the precipitates formed immediately after cessation of $MgCl_2$ dosing (black lines) confirms their amorphous nature. After one week, the precipitates are crystalline. In control runs (a), the main phase found was nesquehonite, while in 1 mM citrate solution the main crystalline phase formed was dypingite.

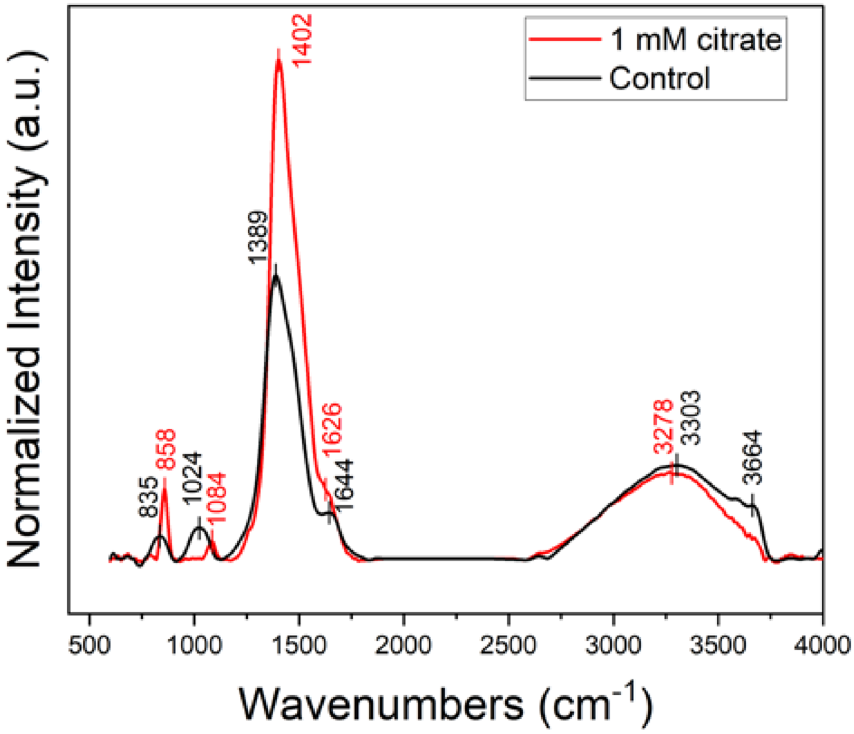

Figure S-4 FTIR spectra of AMC precipitates formed in control (black curve) and sodium citrate (1 mM, red curve) titration runs.

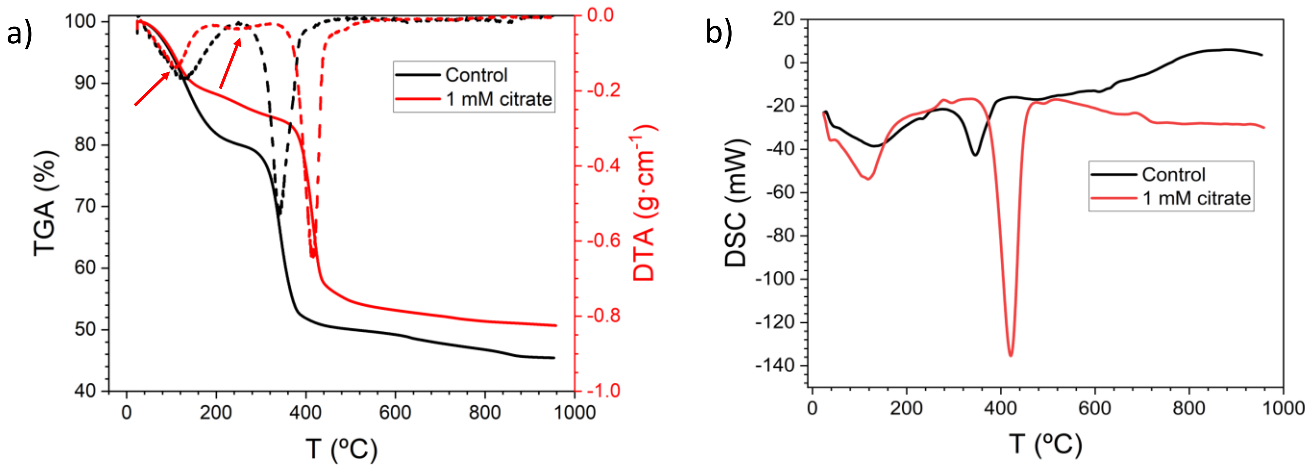

Figure S-5 TGA/DTA **(a)** and DSC **(b)** plots of the precipitates formed in titration runs. Red arrows mark the two dehydration steps observed in the case of citrate-bearing AMC (see main text for further explanation).

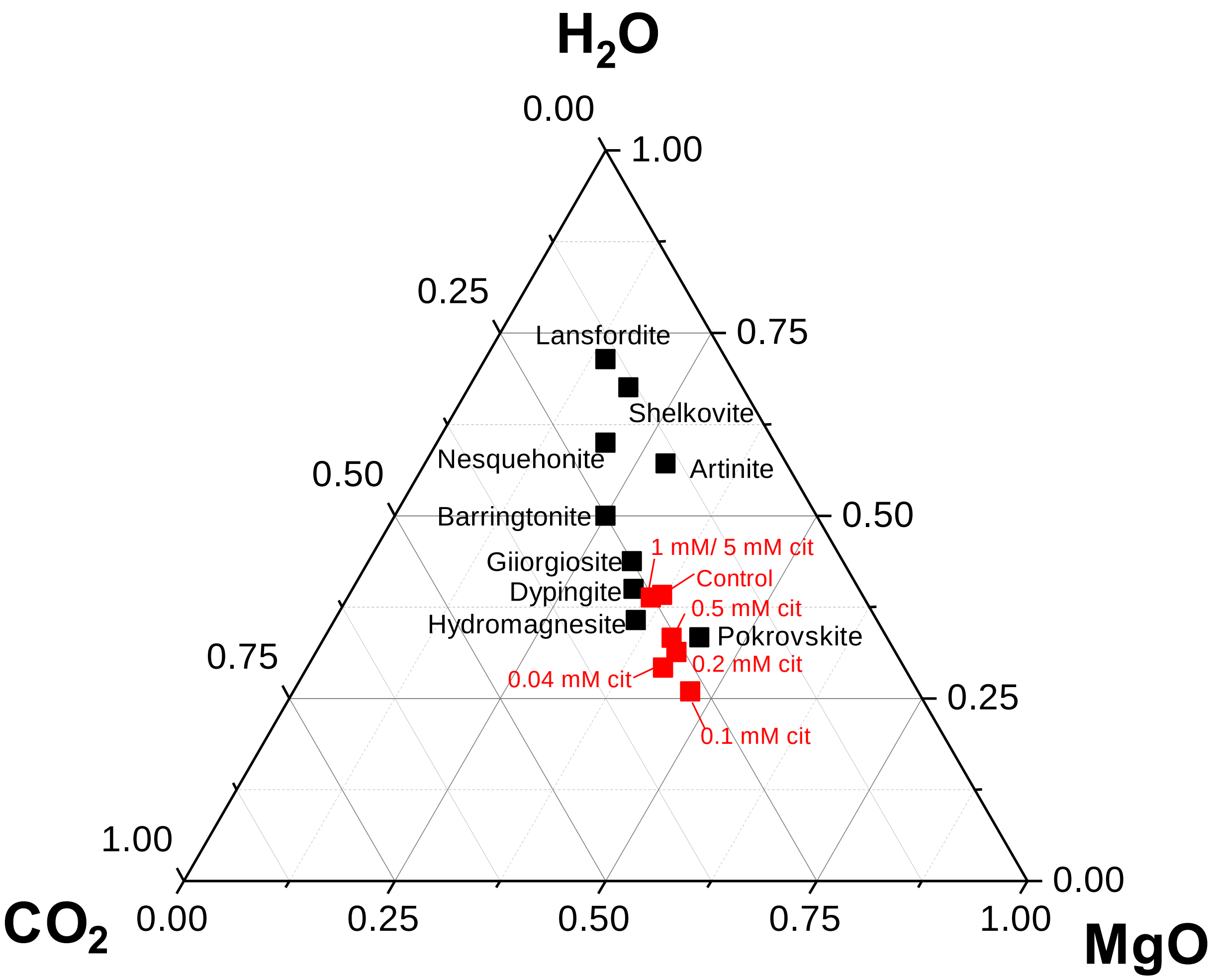

Figure S-6 Ternary phase diagram of the CO_2-MgO-H_2O system, showing hydrated magnesium carbonate minerals (black squares) and AMC samples synthesised in this work (red squares).

Supplementary Tables

	Zeta potential (mV)
AMC control 2010 s	-7.91 ± 0.33
AMC control 15000 s	-5.80 ± 0.16
AMC 5mM citrate 20000s	-3.93 ±0.40
AMC control redispersed in water	-8.54 ± 0.38
AMC 5mM citrate redispersed in water	-6.09 ± 0.51

Table S-1 Zeta potential values of control and citrate-bearing AMC. The values in the first three rows correspond to measurements of aliquots of the reaction medium with dispersed AMC particles collected at different elapsed times during titration. The values in the last two rows correspond to AMC samples dried and redispersed in MilliQ water.

Supplementary Information References

Lide, D.R. (Ed.). (2004) CRC handbook of chemistry and physics (85th ed.). CRC Press LLC, BocaRaton, FL. 2712 pp.

McCleskey, R.B., Nordstrom, D.K., Ryan, J.N., Ball, J.W. (2012) A new method of calculating electrical conductivity with applications to natural waters. *Geochimica et Cosmochimica Acta* 77, 369-382. https://doi.org/10.1016/j.gca.2011.10.031

Ruiz-Agudo, E., Burgos-Cara, A., Ruiz-Agudo, C., Ibáñez-Velasco, A., Cölfen, H., Rodriguez-Navarro, C. (2017) A non-classical view on calcium oxalate precipitation and the role of citrate. *Nature Communications* 8, 1-10. https://doi.org/10.1038/s41467-017-00756-5

Ruiz-Agudo, E., Ruiz-Agudo, C., Di Lorenzo, F., Alvarez-Lloret, P., Ibanez-Velasco, A., Rodriguez-Navarro, C. (2021) Citrate Stabilizes Hydroxylapatite Precursors: Implications for Bone Mineralization. *ACS Biomaterials Science & Engineering* 7, 2346-2357. https://doi.org/10.1021/acsbiomaterials.1c00196